# High-resolution multicontrast tomography with an X-ray microarray anode–structured target source

Guibin Zan[a], Sheraz Gul[b], Jin Zhang[a], Wei Zhao[c], Sylvia Lewis[b], David J. Vine[b,1], Yijin Liu[a,1], Piero Pianetta[a], and Wenbing Yun[b]

[a]Stanford Synchrotron Radiation Lightsource, SLAC National Accelerator Laboratory, Menlo Park, CA 94025; [b]Sigray Inc., Concord, CA 94520; and [c]School of Physics, Beihang University, 100083 Beijing, China

Multicontrast X-ray imaging with high resolution and sensitivity using Talbot–Lau interferometry (TLI) offers unique imaging capabilities that are important to a wide range of applications, including the study of morphological features with different physical properties in biological specimens. The conventional X-ray TLI approach relies on an absorption grating to create an array of micrometer-sized X-ray sources, posing numerous limitations, including technical challenges associated with grating fabrication for high-energy operations. We overcome these limitations by developing a TLI system with a microarray anode–structured target (MAAST) source. The MAAST features an array of precisely controlled microstructured metal inserts embedded in a diamond substrate. Using this TLI system, tomography of a Drum fish tooth with high resolution and tri-contrast (absorption, phase, and scattering) reveals useful complementary structural information that is inaccessible otherwise. The results highlight the exceptional capability of high-resolution multicontrast X-ray tomography empowered by the MAAST-based TLI method in biomedical applications.

Talbot–Lau grating interferometry | microarray anode–structured target | X-ray source | phase-contrast tomography

Adding phase and scattering/darkfield contrast to the conventional absorption contrast in X-ray microscopy is a rapidly expanding research field because it offers tremendous advantages in a wide range of applications. The different contrast mechanisms are highly complementary, as they feature different sample–beam interactions that fingerprint different material properties. For example, the real and imaginary parts of the refractive index exhibit very significant differences in their absolute values (*SI Appendix*, Fig. S1) and represent the phase shift and attenuation of the X-ray, respectively (1–7). This has major implications for biomedical imaging, e.g., mammography (6, 8, 9), lung pathology (10–13), and industrial applications such as the structural investigation of carbon-reinforced polymer composites (14, 15). With this motivation, a variety of X-ray phase-contrast imaging (XPCI) techniques have been developed (2, 5–7, 9, 16), and there is a strong emphasis on achieving the phase-contrast efficiently and quantitatively (17–20). Among all these methods, grating-based XPCI (GXPCI), especially the Talbot–Lau interferometry (TLI) (3), is a leading contender for bringing XPCI into widespread adoption. Its unique advantages include 1) the compatibility with conventional, low-brilliance laboratory X-ray sources (3), 2) high sensitivity at high X-ray energy (20), and 3) desirable spatial resolution down to the micrometer level (21). Furthermore, it simultaneously provides three different contrast mechanisms: attenuation, refraction (differential phase-shift), and scattering (dark-field) in a single GXPCI dataset. The multicontrast modalities of TLI can offer valuable and complementary information for better discrimination of different structural components with different physical properties (4, 19). The GXPCI-enabled scattering contrast corresponds to the ultra-small-angle scattering strength of a material and offers excellent sensitivity to the morphological features that are much finer than the nominal spatial resolution (22–24). The phase-contrast component, on the other hand, quantitatively

reconstructs the spatial distribution of the electron density, which is a fundamental material property that has different implications in different applications (20, 25). For example, the electron density of a battery cathode material fingerprints its state of charge and evolves as the battery is charged and discharged (26). Therefore, the three-dimensional (3D) electron density map of a battery electrode can be used to quantify the reaction heterogeneity, which is critical to the battery performance. The extraordinary potential of TLI tomography is reflected by the broad interest in applying this method to biological and medical imaging (5, 6, 8, 9, 12, 13), nondestructive testing (14, 27), materials science (19), and security screening (28). There are, however, key limitations of this technique that have yet to be addressed.

A main advantage of TLI is its compatibility with a high-power laboratory X-ray source, which could largely improve the throughput of the experiment (3). In a conventional TLI setup, an absorption source grating (G0) is utilized to formulate a structured illumination pattern (Fig. 1*A*). G0 is inserted near the exit window of the X-ray tube for improving the spatial coherence and for reinforcing a geometrical constraint that matches the configuration of the downstream optics (*SI Appendix*, Fig. S2). The drawback of using the source grating G0 is that more than half of the X-ray's source flux is wasted, significantly jeopardizing the efficiency of the imaging system. To increase the imaging sensitivity, one needs to use G0 gratings with fine periods as small as a few micrometers (29).

**Significance**

Talbot–Lau interferometry (TLI) holds remarkable potential for multicontrast X-ray imaging but suffers from technical challenges associated with microfabrication and limited efficiency. We tackle the frontier challenges in this field by developing a microarray anode–structured target source with a built-in structured illumination scheme. Our development facilitates high-resolution and high-sensitivity TLI imaging without the absorption source grating. We demonstrate the tri-contrast tomography capability with a Drum fish tooth specimen and separate the biological features with different combinations of physical properties. Our approach not only addresses the long-standing challenges in the field of X-ray TLI phase-contrast imaging but also features a compact setup that can potentially be made broadly available to academia research and industrial applications.
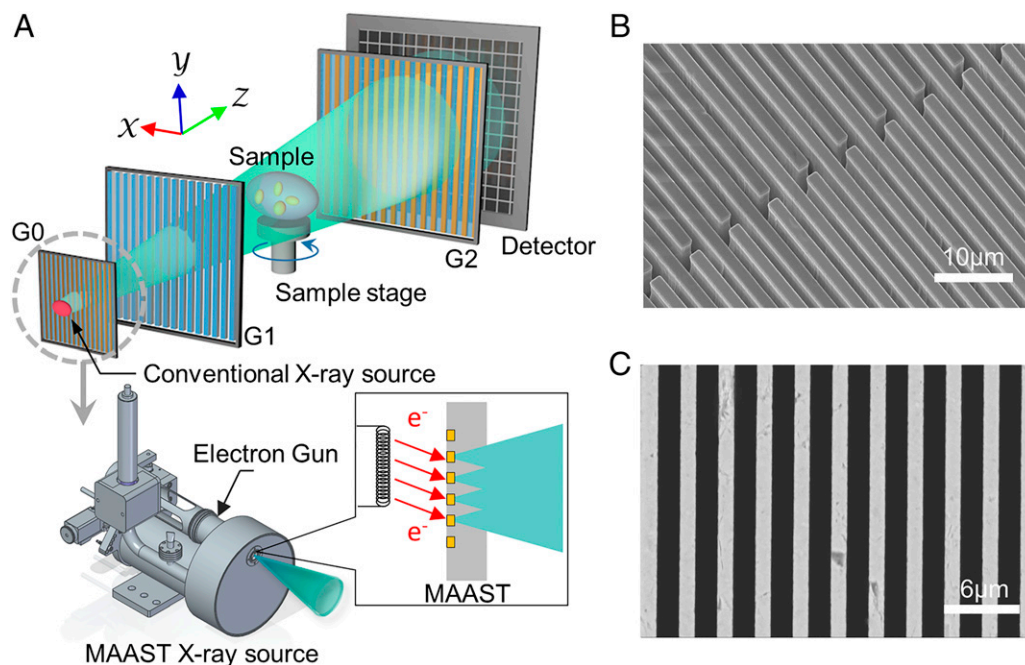
**Fig. 1.** Schematic comparison of the conventional TLI setup and our approach with a MAAST source is shown in *A*. SEM images of the MAAST pattern with etched grooves (*B*) and with W-MMIs embedded in the polycrystalline diamond substrate (*C*).

Meanwhile, to ensure a sufficient X-ray transmission contrast, the thickness of the G0 grating lines has to reach several tens of micrometers, manifesting a desire for a high aspect ratio (AR) that is technically very challenging (30). To overcome this issue, Thüring et al. tilted the gratings with respect to the beam to effectively increase the AR. This approach, however, significantly reduces the useful field of view (FOV), compromising the practicality of this technique (30). Additionally, a G0 with large AR collimates the X-ray beam, which is another reason for the diminished FOV ($\propto$AR$^{-1}$) (*SI Appendix*, Fig. S3) (21). We acknowledge that curved and tiled gratings can potentially be fabricated to alleviate this issue; however, they are associated with great challenges in microfabrication, particularly when targeting high a AR and small radius (21, 31). Several approaches have been introduced to circumvent the use of G0 and its associated limitations. One demonstrated approach involves fabricating grooves on an anode target for structured illumination. However, this method has a rather limited FOV because the spatial coherence property changes as a function of the target position (32). Morimoto et al. developed a TLI with a transmission grating by using a structured X-ray source. They demonstrated two-dimensional imaging results with a rather low spatial resolution and at a low working energy (20 kV) (33, 34). Despite the tremendous research efforts devoted to this field, the aforementioned challenges have hindered the broad adoption of TLI as a standard tool for high-resolution structural investigations with high-energy X-rays.

To tackle these challenges, we developed a TLI system with a microarray anode–structured target (MAAST) X-ray source. We overcome the limitations of the conventional configuration with an extended source and a G0 grating by designing and incorporating the illumination pattern into the MAAST source as a built-in feature. Our approach significantly improves the efficiency in the use of source X-rays for imaging at high resolution and with high sensitivity. We further present correlative tri-contrast tomography on a Drum fish tooth specimen and demonstrate a clear separation of biological features with different physical properties. Our results highlight the exceptional imaging capability empowered by the MAAST-based TLI method. Our approach also features a compact

and robust setup that can potentially be made broadly available to academia research and industrial applications.

## Results

**Modulating the Illumination Pattern with Highly Efficient MAAST.** As it has been elaborated above, a conventional TLI setup utilizes an absorption source grating G0 for defining the illumination pattern (Fig. 1 *A*, *Top*), which, unfortunately, comes with decreased efficiency as well as the technical challenges in microfabrication. We tackle this challenge by eliminating the source grating and, instead, build the desired pattern into the anode target. Our MAAST X-ray source (Fig. 1 *A*, *Bottom*) features an array of precisely controlled microstructure metal inserts (MMI) that are embedded in a diamond substrate. These MMIs act as X-ray generators and collectively form a desired illumination pattern (see illustrations in Fig. 1 *B* and *C*). Upon irradiating the MAAST with electrons, X-rays emit from the other side of the diamond substrate and were used for imaging.

While the illumination pattern can be defined by the shape and arrangement of the MMIs, the contrast relies on the difference between the efficiency of X-ray generation from the MMI and that from the substrate. To maximize X-ray production in the MMIs, the MMI materials shall have a high atomic number, a high mass density, a high thermal conductivity, and a high melting point. With these considerations, the options were narrowed down to W, Mo, and Cu. For the results presented below, we choose tungsten as our MMI material (see *Materials and Methods* for more details) because of its high bremsstrahlung production rate (35). As for the substrate, diamond is chosen because it holds several favorable properties that not only minimize its X-ray production but also provide sufficient mechanical support and good thermal conductivity (2,200 W · mK$^{-1}$) that efficiently dissipate the heat generated by the incident electrons (36). Further numerical optimization of the MAAST X-ray source for specific TLI setups was carried through Monte-Carlo simulations, and the details can be found in our earlier reports (37, 38). More discussions about the feasibility and advantages of operating our MAAST at even higher X-ray energies are included in the *SI Appendix*.

www.manaraa.com

**TLI with MAAST.** Based on our MAAST source, we designed a TLI system for X-ray imaging and tomography with high spatial resolution and sensitivity (*SI Appendix*, Fig. S4). Details about the TLI and the configuration of our specific imaging system can be found in the *SI Appendix*. Prior to imaging real-world specimens, we carefully characterized our setup in several key aspects that are crucial to the multimodal imaging experiments. Upon exposure to the electron beam, the MAAST emits X-rays that are specific to the MMI material. The MAAST emission spectrum shows a good consistency with the theoretical prediction (see *Materials and Methods* for more experimental details), confirming the efficiency of the electron irradiation on the structured W anode (Fig. 2*A*). The MAAST X-ray source provides an X-ray flux of ∼2 to 4 × 10$^{11}$ photons/s/sr with a focal spot in the range of tens of microns, which is about two times greater than that of a typical X-ray microfocus source. The outstanding thermal properties of the diamond substrate play a key role in improving the MAAST's X-ray flux (39). We further monitored the X-ray intensities from the MAAST source over time for evaluating the stability of the system. The stability assessment was conducted under three different application-relevant conditions: 1) with direct charge-coupled device (CCD) exposure, 2) with a 2-mm-diameter pinhole at the exit window, and 3) with a 15-μm Silver filter. As shown in Fig. 2*B*, the MAAST source demonstrates remarkable stability with negligible standard deviation (SD) in the intensity variation over 6 h. To optimize the setup for studying different specimens with different properties, three different configurations have been designed and calibrated for different combinations of X-ray energy and sensitivity (*SI Appendix*, Table S1). Fundamentally, the performance of the

TLI system relies on the visibility of the phase-stepping curve (PSC), which represents the intensity variation as the detector grating (G2) is scanned with respect to the phase grating (G1) (see Fig. 2 *C*, *Inset* for the definition of the visibility) (29, 40). This is because the phase retrieval from the TLI imaging data is essentially a quantification of the sample-induced distortions in the PSC, and, therefore, the ultimate signal-to-noise ratio of the imaging data is positively correlated with the visibility of the PSC (29). We show in Fig. 2*C* the experimentally measured PSC visibility map over an ∼10 × 10 mm$^2$ area with the corresponding histograms plotted in Fig. 2*D*. All the visibility measurements were performed with 11-step phase stepping and with an exposure time of 15 s per exposure. The visibility over the measured FOV is rather homogeneous, with a mean value at ∼30%. This value changes slightly as a function of X-ray energy (Fig. 2*D*) but remains at an excellent level (41, 42). We further evaluate the setup's angle sensitivity by means of the smallest detectable refraction angle (29). The angle sensitivities are 256, 165, and 287 nano-radian (nrad) for the three different configurations, respectively. It worth pointing out that our setups are designed with considerations on a balance between the engineering practicality and the desired performance (e.g., resolution and sensitivity). The asymmetric system (Setup 3 in *SI Appendix*, Table S1) has a lower sensitivity, which is purposely designed to work with a large-period G2 absorption grating. Generally, our system provides a higher sensitivity compared with other micro-resolution setups with similar system lengths (41). Our improvements largely benefit from the high visibility of our PSC, which is a result of the use of the herein-developed MAAST. We acknowledge that a much higher sensitivity (5 nrad) has been reported using a
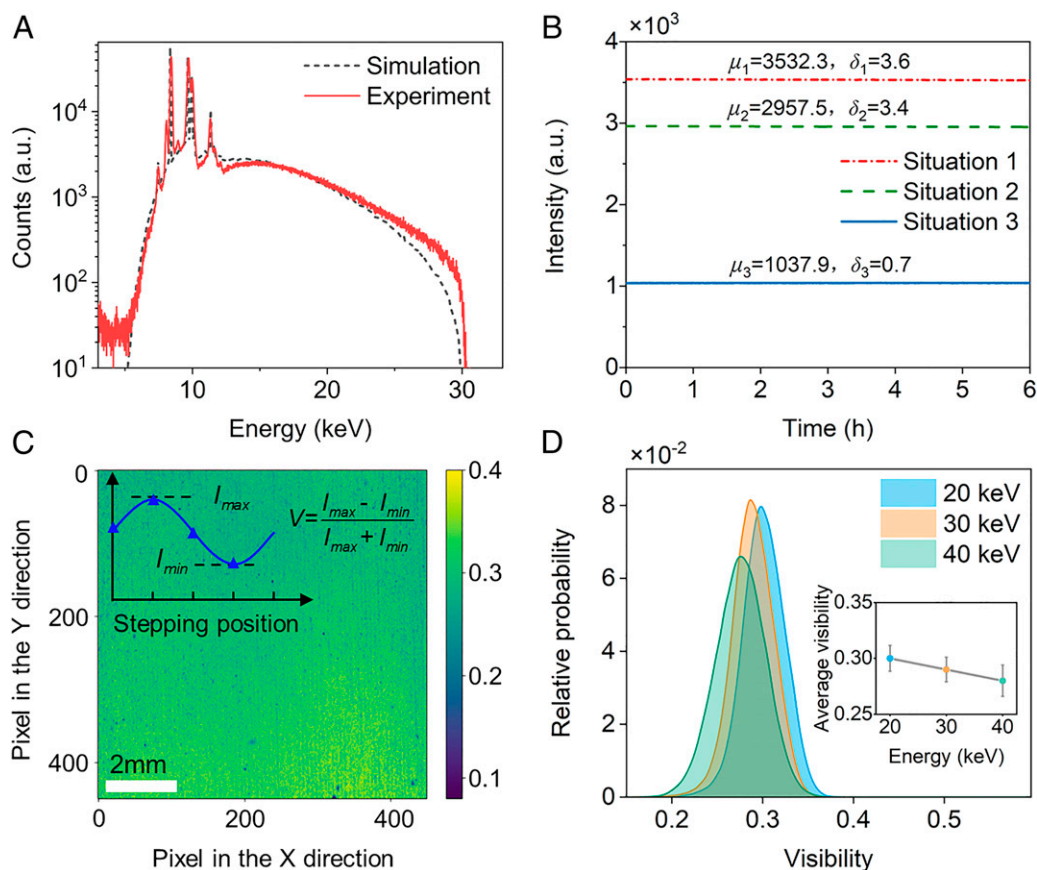
**Fig. 2.** Characterization of the developed imaging system. (*A*) The X-ray spectrum emitted from the W-MAAST source. (*B*) The intensity variation over time. $\mu_1$, $\mu_2$, and $\mu_3$ are the mean values and $\delta_1$, $\delta_2$, and $\delta_3$ are the SDs over the measured time (*C*) The visibility map measured with Setup 1. (*D*) The probability distribution of the visibility at different X-ray energies over the FOV. The error bar is the SD value.

Zan et al.
High-resolution multicontrast tomography with an X-ray microarray anode–structured target source

www.manaraa.com

long (~1.72 m) laboratory TLI setup by coupling a large X-ray spot of 100 μm and, thus, much higher X-ray flux, with a high-efficiency single-photon–counting X-ray detector with much larger pixels (172 μm) (20). It is not the intent of this work to push our effort to pursue the highest sensitivity but rather to develop a MAAST-based TLI setup that is robust, efficient, compact, and practical. It should be noted that a MAAST-based TLI setup could offer advantages in imaging sensitivity over the conventional TLI due to its high visibility and high flux (see *SI Appendix* for detailed discussion).

**Tri-contrast X-Ray Imaging and Tomography with MAAST.** With our MAAST-based TLI system calibrated, we demonstrate tri-contrast X-ray imaging and tomography with a Drum fish tooth specimen using Setup 1 in *SI Appendix,* Table S1. The tri-contrast imaging is achieved by conducting phase stepping and, subsequently, analyzing the difference in the PSCs with and without the sample in place. The maps of sample-induced absorption, refraction, and scattering are extracted and presented in Fig. 3 *A–C*, respectively. A direct visual assessment of these maps suggests that these maps exhibit very significant differences in their sensitivity to different sample properties (as illustrated by Fig. 3 *A–C*, Insets). To further understand these differences, we plot line profiles across the sample (as annotated in Fig. 3*A*) over these maps. The absorption line profile (black curve in Fig. 3*D*) features a strong baseline that is predominantly caused by the thickness of the sample in the beam direction. The intensity variations caused by the fine structural features are significantly weaker than the baseline. The refraction and scattering signals (red and blue curves in Fig. 3*D*), on the other hand, have a largely suppressed background with the high-spatial-frequency features enhanced. The refraction signal has positive and negative values due to the directional sensitivity, while the scattering signal is proportional to the absolute scattering power and is nondirectional.

We further plot the relative histograms of these three maps in Fig. 3*E*. It is interesting to note that, while the refraction histogram is fairly symmetric with respect to its peak position (red curve in Fig. 3*E*), both the absorption and the scattering signals exhibit asymmetry in their histograms (black and blue curves in Fig. 3*E*). The spread of the histogram curve reflects the effectiveness in the utilization of the data's dynamic range. The absorption and the scattering histograms demonstrate relatively sharper cutoffs on different sides of the curve, indicating their different effectiveness in handling weak and strong signals. We further compare the Fourier power spectra of these three maps in Fig. 3*F*, which clearly illustrates that the absorption map highlights the low-spatial-frequency features, while the refraction and scattering maps enhance the high-spatial-frequency components. The tri-contrast imaging data are further acquired as the sample is rotated in a tomographic scan (see *Materials and Methods* for more experimental details). The reconstructed tri-contrast tomograms over a representative slice through the center of the imaged Drum fish tooth specimen and their respective Fourier transformed patterns are shown in *SI Appendix,* Fig. S5. It is interesting to note that two types of signals coexist and overlap in the Fourier patterns: a rather scattered pattern and a set of more-defined radial spikes. The scattered pattern is correlated with the disordered structural features, and the radial spikes are associated with the radial structural features. Our results suggest that, in this particular sample, the refraction signal emphasizes the disordered structural features, and, in contrast, the scattering signal highlights the ordered radial features. The observation of different structural features in the images of different contrast mechanisms is very interesting and could lead to useful scientific interpretations. For example, while both of the μ and δ are associated with the electron density, they are not simply correlated, and the local dissociation between the two could be utilized to identify features of interest that might be overlooked
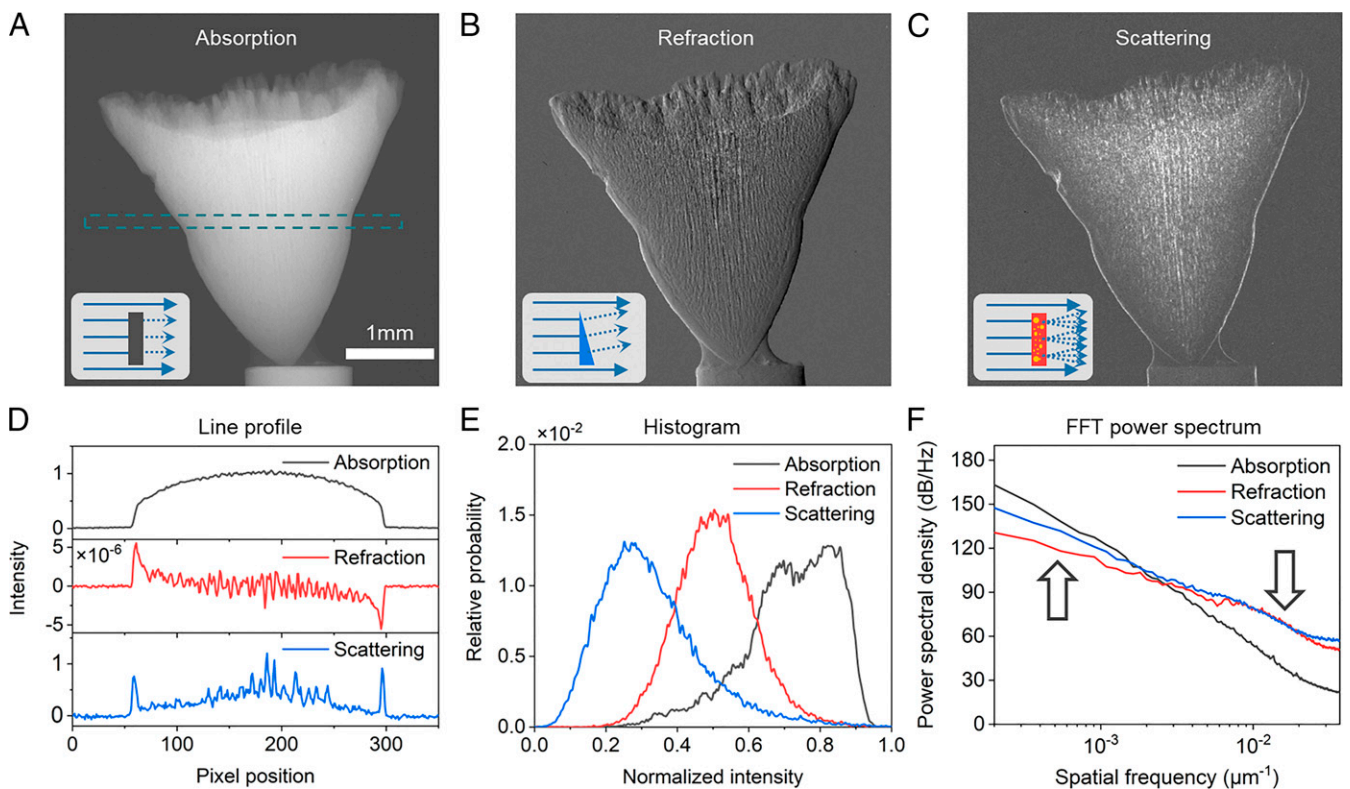


**Fig. 3.** The tri-contrast X-ray imaging results of a fish tooth specimen. (*A–C*) The maps of absorption, refraction, and scattering, respectively. The display windows of *A–C* are $[-0.1, 1.2]$, $[-5.5 \times 10^{-6}, 5.5 \times 10^{-6}]$, and $[-0.1, 1.3]$, respectively. (*D*) The intensity profile over these three maps across the horizontal line as annotated in *A*. (*E*) The histograms of these maps. (*F*) The Fourier power spectra of these maps.

otherwise. A more in-depth analysis relies on domain knowledge specific to the sample and is beyond the scope of this paper.

**Tri-contrast Tomography and Data Clustering Empowered Biological Feature Identification.** The correlative tri-contrast tomography offers an excellent opportunity for distinguishing biological features with different physical properties. With the tri-contrast tomographic results as inputs, we carry out unsupervised data classification using the K-mean clustering method. Based on the local physical properties, all the real-space voxels in the scanned 3D volume can be plotted into a 3D space (Fig. 4 *B*, *C*, and *D*) defined by the absorption ($\mu$), refraction ($\delta$), and linear diffusion ($\varepsilon$) coefficients. The clustering algorithm divides all the real-space voxels into five different categories based on the similarity in the respective values of $\mu$, $\delta$, and $\varepsilon$. As shown in Fig. 4 *A* and *E*, these clusters also feature very distinct spatial distributions. Cluster 4 shows strong signals in all three parameters, matching the characteristics of the cellular cementum (43, 44). Cluster 1 shows strong signals in $\mu$ and $\delta$ as well as a relatively low $\varepsilon$ value, indicating a rather large gradient in the local density distribution that often constitutes a boundary between different structural components in the biological system. Cluster 1 appears on the outer surface of the cellular cementum; it is therefore attributed to the acellular cementum, which is more calcified. The difference in the respective physical properties of cellular and acellular cementum is rather small, causing challenges in distinguishing them using conventional tomography data. Our result provides an approach that harnesses the correlative tri-contrast tomography data for precise cementum recognition. The dentin is primarily constituted of clusters 2, 3, and 5. As shown in Fig. 4*C*, clusters 2, 3, and 5 exhibit a positive correlation between $\mu$ and $\delta$, which suggests that the dense dentine features are confined to rather localized regions with a sharp boundary. A negative correlation between $\varepsilon$ and $\mu$ can be observed for clusters 2, 3, and 5 (Fig. 4*D*). It hints that the fine structural features that are smaller than the nominal spatial resolution are ubiquitous in the dentine. These results highlight the exceptional tri-contrast tomography capability that is empowered by the MAAST-based TLI method. With our method that leverages advanced experimental and computational capabilities, we demonstrate the separation of Drum fish tooth features of different physical properties with high resolution and sensitivity. This approach could facilitate detection and provide a better understanding of the cementum calcification, which could subsequently offer important clinical implications.

## Discussion

The TLI holds remarkable potential for multicontrast X-ray imaging but suffers from technical challenges associated with the microfabrication and the limited efficiency. Despite the tremendous research efforts in this field, the broad adoption of TLI in industrial and medical applications is yet to be realized. In this work, we tackle the frontier challenges in this field by developing a MAAST source with a built-in structured illumination scheme. Our development facilitates high-resolution and high-sensitivity TLI imaging without the use of an absorption source grating. We demonstrate the tri-contrast tomography capability with a Drum fish tooth specimen and separate the biological features with different combinations of physical properties. Our approach not only addresses the long-standing challenges in the field of X-ray TLI phase-contrast imaging but also features a compact, robust, and practical setup that can potentially be made broadly available to academia research and industrial applications (*SI Appendix*, Fig. S4).

In the presented data, the exposure time is relatively long and is limited by the low efficiency of the detector used (with an objective lens of small numerical aperture at 0.055 and a thin scintillator at 80 μm thick). The total exposure time of our experiment can be significantly reduced simply by using a more efficient detector with an objective lens of a large numerical aperture (at 0.1) and a 200-μm-thick scintillator, which is now being implemented as an upgrade to our system. Another promising avenue is to incorporate the state-of-the-art photon-counting detectors for suppressing the imaging noise as much as possible to Poisson statistics. Furthermore, we acknowledge that some advanced acquisition and processing scheme of tri-contrast tomography has been demonstrated (45) and can be integrated into our system for further improving the efficiency. Another possible strategy to improve the efficiency is
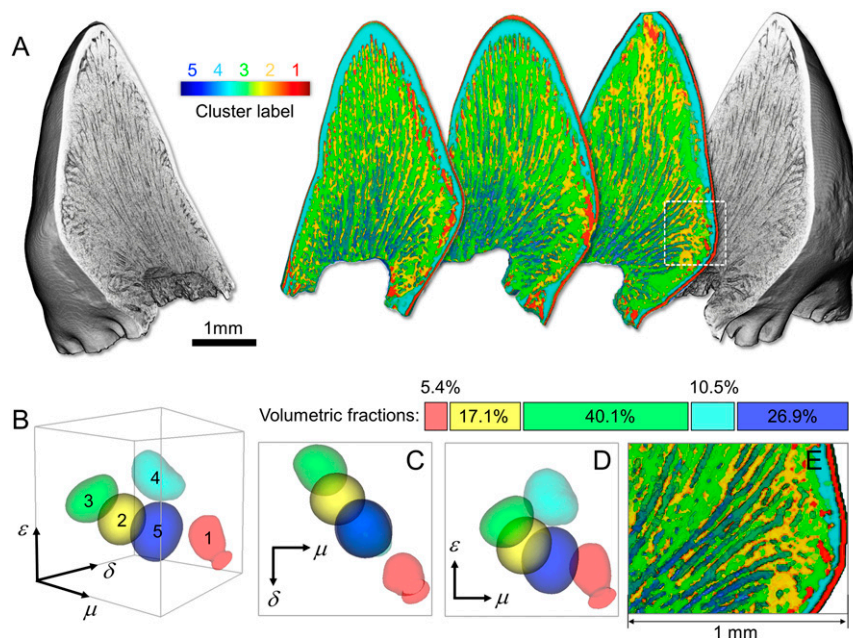


**Fig. 4.** Tri-contrast tomography facilitated data clustering and segmentation. (*A*) The 3D rendering of the tomographic result (grayscale in the left and right), with a few virtual slices color coded to the data classification results. *B–D* illustrate the different properties of the five different data clusters. (*E*) A magnified view of the white rectangle in *A*.

Zan et al.
High-resolution multicontrast tomography with an X-ray microarray anode–structured target source

www.manaraa.com

to increase the power loading, which could compromise the ultimate spatial resolution and shall be carefully considered based on the specific applications. In terms of the source lifetime and long-term stability, we declare that this particular MAAST source has been operated for routine experiments in our laboratory for more than a year, and we do not observe any obvious degradation in the performance of MAAST. Based on the experiments on our TLI protype, the fluctuation of the ambient temperature exhibits a significant impact on the stability of entire system. Therefore, a temperature-management system could be crucial for the time-consuming experiments (e.g., tri-contrast tomography). For a broad application to research laboratories and the industry, engineering efforts are needed to stabilize the system to the highest extent. On the other hand, the real-time position monitor (e.g., laser interferometer–based position encoder) could be useful for correcting any errors induced by the imperfections of the hardware setup during the data reduction process.

## Materials and Methods

**Detailed Design of the Tungsten-Based MAAST.** The tungsten-based MAAST (W-MAAST) pattern with an area of $0.4 \times 0.4$ mm was embedded in a polycrystalline diamond substrate with a 10-mm diameter and 1-mm thickness. The transmission targets are patterned using conventional photolithography and reactive ion etching processes. A scanning electron micrograph (SEM) of the pattern with etched grooves is shown in Fig. 1*B*. The period of the W-MMIs is 3.0 μm, and the duty cycle is 0.33, giving 1.0-μm width tungsten lines separated by 2.0 μm of the diamond. The depth of the W-MMI along the surface normal was optimized using continuous slowing-down approximation to estimate the maximum travel range of the electrons in the matter (46). Furthermore, tungsten is embedded in the trenches through chemical vapor deposition and surface polishing. Fig. 1*C* shows an SEM image of the fabricated W-MAAST embedded in the polycrystalline diamond substrate. The line and space pattern in the W-MAAST can be clearly distinguished. Finally, a capping layer of a few nanometers is sputter coated over the diamond substrate to provide uniform electrical conductivity. In our system, the focus size of the electron beam can be adjusted between $50 \times 50$ μm$^2$ and $6 \times 6$ μm$^2$, offering flexibility to the imaging experiments. The acceleration voltage of the electron gun can be operated over a range of 20 to 70 kV.

**MAAST Characterization and Simulation.** The X-ray MAAST source was operated with a 30-kV tube voltage and 1.34-mA tube current. We compare the X-ray spectra from the Monte Carlo simulation and the one experimentally measured using a silicon drift detector (KETEK, Inc.) (Fig. 2*A*). The X-ray spectrum simulation was conducted using Geant4 (37, 38, 47). We conducted correction for air attenuation, exit window attenuation, and energy-dependent absorption of the spectrometer's sensor material to ensure the accuracy. The characteristic peaks of tungsten match the theoretic values, confirming that the MAAST was irradiated by the electron beam. The spectra produced by the X-ray MAAST source with different voltages and different currents were measured (*SI Appendix*, Fig. S6). We do not include higher voltages because the upper limit in the working range of our silicon drift detector is 40 kV. The TLI is compatible with X-rays with a relatively wide energy bandwidth ($\Delta E/E > 10\%$) (3, 29). However, the X-ray bandwidth directly affects the visibility of the interference pattern. In our experiment, an Ag filter was used to reject low-energy photons for improving the visibility. The majority of the X-ray photons are produced by the MMIs of the MAAST (*SI Appendix*, Fig. S7). This is the fundamental reason for the improved PSC visibility in our setup.

To understand the stability of the transmission MAAST source, the X-ray intensities were measured as a function of time under three different application-relevant conditions. The detector was located downstream 218 mm from the source focus. The X-ray intensities of the MAAST source are recorded with an in-house CCD-based detector by a series of integration exposures of 15 s.

**Detailed Imaging System Configuration.** An X-ray TLI was constructed with an in-house fabricated MAAST X-ray source as an illumination system for TLI, a G1 and G2, and a scintillator-based X-ray detector. The detector used consists of 80-μm-thick Cesium Iodide (Thallium) (e.g., CsI [Tl]) scintillator, a 2× optical lens system, and a CCD camera (Andor Technology, Ltd) with 2,048 × 2,048 pixels (pixel size at 13.5 μm). The minimum achievable effective pixel size ($p_s$) on the sample plane depends on the focus size of the source and the pixel size of the detector. Depending on the detector system, the spatial resolution is $\Delta x \geq p_s$. The combination of the MAAST source and in-house detector offers a minimum achievable effective pixel size of 4.4 to 10.6 μm, which is in the resolution range of a typical high-resolution micro-CT (computed tomography) system (42). In the initial experiment, the setup had a FOV of 6.5 mm, limited by the detector size, and a geometric magnification of 1.8 (*SI Appendix*, Fig. S4). The design method of TLI combined with the X-ray MAAST source is presented in *SI Appendix*. The detailed setup parameters are listed in *SI Appendix*, Table S1. Two different TLI configurations were employed at three different X-ray energies; one makes use of a symmetric mode, and the other employs an inverse geometry mode. The symmetric configuration has the highest angular sensitivity for a given system length (48). Two symmetric setups work in third Talbot order at an X-ray energy of 20 keV and 30 keV, respectively. The inverse geometry configuration removes the fabrication difficulty of G2 with an available pitch for a large geometry magnification, where the distance between X-ray source and phase grating is shorter than the distance between phase grating and an X-ray detector (48, 49). The inverse geometry setup was acquired in the first Talbot order using an effective X-ray energy of 40 keV.

**Tomography.** Today's commercial laboratory-based micro-CT scanners have a key role to play in 3D imaging, offering a high resolution to probe the secrets of matter in even greater detail for various kinds of specimens. The further integration of tabletop X-ray micro-CT scanners with TLI to acquire phase and scattering contrast images can dramatically enhance their range of applications, from biological samples to advanced composite material to geological material, for both industrial and research applications. To perform CT scans to obtain the 3D information of the materials, the specimen is rotated around the rotation axis, and a phase stepping series is recorded for each projection angle. The tri-contrast images were extracted by Fourier analysis of the intensity oscillation curves in each detector pixel (40). A graphics processing unit (GPU)-based Feldkamp–Davis–Kress (FDK) cone-beam filtered back-projection (FBP) reconstruction code developed in the house was used to reconstruct the three contrast images. The reconstruction of the linear diffusion coefficient related to dark-field contrast is processed in the same way as the reconstruction of the attenuation coefficients using a standard FBP with a Ram-Lak filter (23). The real part of the X-ray refractive index related to differential phase contrast is directly reconstructing the 3D volume dataset from the differential phase-contrast projections by using a Hilbert filter in the FBP reconstruction (50). It should be noted that the reconstruction with the Hilbert filter is in fact an integral reconstruction.

To improve the spatial resolution, the focal spot of the MAAST X-ray source in the presented system was set to 14 μm, and the detector pixel size is $13.5 \times 13.5$ μm$^2$. The reconstructed voxel size is close to 7.9 μm under the configuration of Setup 1. The power loading of the MAAST X-ray source was set to 35 W. In this experiment, G2 was displaced with a step of $p_2/5$ in the phase stepping procedure, and five images were acquired sequentially in any given viewing angle with an exposure time of 30 s for each image. The whole CT scan consisted of 611 viewing angles over 183°. It took ~26 h in total. Owing to the G1 and G2, the TLI is very sensitive to the mechanical drift of any components in the system. To address this issue, frequent acquisition of the flat-field background images is a common approach (42). In the presented experiment, the projections are corrected with the closest flat-field background images, which are acquired every 20°.

**Data Availability.** All study data are included in the article and/or *SI Appendix*.

1. A. Momose *et al.*, Demonstration of X-ray talbot interferometry. *Jpn. J. Appl. Phys.* **42**, L866–L868 (2003).
2. A. Momose, Recent advances in X-ray phase imaging. *Jpn. J. Appl. Phys.* **44**, 6355–6367 (2005).
3. F. Pfeiffer, T. Weitkamp, O. Bunk, C. David, Phase retrieval and differential phase-contrast imaging with low-brilliance X-ray sources. *Nat. Phys.* **2**, 258–261 (2006).
4. F. Pfeiffer *et al.*, Hard-X-ray dark-field imaging using a grating interferometer. *Nat. Mater.* **7**, 134–137 (2008).
5. A. Bravin, P. Coan, P. Suortti, X-ray phase-contrast imaging: From pre-clinical applications towards clinics. *Phys. Med. Biol.* **58**, R1–R35 (2013).
6. S. T. Taba *et al.*, X-ray phase-contrast Technology in breast imaging: Principles, options, and clinical application. *AJR Am. J. Roentgenol.* **211**, 133–145 (2018).

www.manaraa.com

7. A. Momose, X-ray phase imaging reaching clinical uses. *Phys. Med.* **79**, 93–102 (2020).
8. Z. Wang *et al*., Non-invasive classification of microcalcifications with phase-contrast X-ray mammography. *Nat. Commun.* **5**, 3797 (2014).
9. L. Heck, J. Herzen, Recent advances in X-ray imaging of breast tissue: From two- to three-dimensional imaging. *Phys. Med.* **79**, 69–79 (2020).
10. S. Schleede *et al*., Emphysema diagnosis using X-ray dark-field imaging at a laser-driven compact synchrotron light source. *Proc. Natl. Acad. Sci. U.S.A.* **109**, 17880–17885 (2012).
11. F. G. Meinel *et al*., Lung tumors on multimodal radiographs derived from grating-based X-ray imaging–a feasibility study. *Phys. Med.* **30**, 352–357 (2014).
12. K. Scherer *et al*., X-ray dark-field radiography–In-vivo diagnosis of lung cancer in mice. *Sci. Rep.* **7**, 402 (2017).
13. K. Willer *et al*., X-ray dark-field imaging of the human lung-A feasibility study on a deceased body. *PLoS One* **13**, e0204565 (2018).
14. N. Morimoto *et al*., Talbot-Lau interferometry-based x-ray imaging system with re-tractable and rotatable gratings for nondestructive testing. *Rev. Sci. Instrum.* **91**, 023706 (2020).
15. V. Revol *et al*., Laminate fibre structure characterisation of carbon fibre-reinforced polymers by X-ray scatter dark field imaging with a grating interferometer. *NDT Int.* **58**, 64–71 (2013).
16. S. W. Wilkins *et al*., On the evolution and relative merits of hard X-ray phase-contrast imaging methods. *Philos. Trans. A. Math. Phys. Eng. Sci.* **372**, 20130021 (2014).
17. P. Zhu *et al*., Low-dose, simple, and fast grating-based X-ray phase-contrast imaging. *Proc. Natl. Acad. Sci. U.S.A.* **107**, 13576–13581 (2010).
18. H. Miao *et al*., Motionless phase stepping in X-ray phase contrast imaging with a compact source. *Proc. Natl. Acad. Sci. U.S.A.* **110**, 19268–19272 (2013).
19. A. Sarapata *et al*., Multi-contrast 3D X-ray imaging of porous and composite mate-rials. *Appl. Phys. Lett.* **106**, 154102 (2015).
20. L. Birnbacher *et al*., Experimental realisation of high-sensitivity laboratory X-ray grating-based phase-contrast computed tomography. *Sci. Rep.* **6**, 24022 (2016).
21. T. Thüring *et al*., High resolution, large field of view X-ray differential phase contrast imaging on a compact setup. *Appl. Phys. Lett.* **99**, 041111 (2011).
22. W. Yashiro, Y. Terui, K. Kawabata, A. Momose, On the origin of visibility contrast in x-ray Talbot interferometry. *Opt. Express* **18**, 16890–16901 (2010).
23. M. Bech *et al*., Quantitative x-ray dark-field computed tomography. *Phys. Med. Biol.* **55**, 5529–5539 (2010).
24. S. K. Lynch *et al*., Interpretation of dark-field contrast and particle-size selectivity in grating interferometers. *Appl. Opt.* **50**, 4310–4319 (2011).
25. A. Sarapata *et al*., Quantitative electron density characterization of soft tissue sub-stitute plastic materials using grating-based x-ray phase-contrast imaging. *Rev. Sci. Instrum.* **85**, 103708 (2014).
26. Z. Jiang *et al*., Machine-learning-revealed statistics of the particle-carbon/binder de-tachment in lithium-ion battery cathodes. *Nat. Commun.* **11**, 2310 (2020).
27. M. Kageyama *et al*., X-ray phase-imaging scanner with tiled bent gratings for large-field-of-view nondestructive testing. *NDT Int.* **105**, 19–24 (2019).
28. E. A. Miller, T. A. White, B. S. McDonald, A. Seifert, Phase contrast x-ray imaging signatures for security applications. *IEEE Trans. Nucl. Sci.* **60**, 416–422 (2013).
29. T. Thüring, M. Stampanoni, Performance and optimization of X-ray grating inter-ferometry. *Philos. Trans. A. Math. Phys. Eng. Sci.* **372**, 20130027 (2014).
30. T. Thüring, M. Abis, Z. Wang, C. David, M. Stampanoni, X-ray phase-contrast imaging at 100 keV on a conventional source. *Sci. Rep.* **4**, 5198 (2014).
31. T. J. Schröter *et al*., Large field-of-view tiled grating structures for X-ray phase-contrast imaging. *Rev. Sci. Instrum.* **88**, 015104 (2017).
32. A. Momose, W. Yashiro, H. Kuwabara, K. Kawabata, Grating-based X-ray phase im-aging using multiline X-ray source. *Jpn. J. Appl. Phys.* **48**, 076512 (2009).
33. T. Shimura *et al*., Hard x-ray phase contrast imaging using a tabletop Talbot-Lau in-terferometer with multiline embedded x-ray targets. *Opt. Lett.* **38**, 157–159 (2013).
34. N. Morimoto *et al*., X-ray phase contrast imaging by compact Talbot-Lau interfer-ometer with a single transmission grating. *Opt. Lett.* **39**, 4297–4300 (2014).
35. E. B. Podgoršak, *Radiation Physics for Medical Physicists* (Springer, Berlin, ed. 2, 2010).
36. S. Kidalov, F. Shakhov, Thermal conductivity of diamond composites. *Materials* **2**, 2467–2495 (2009).
37. G. Zan *et al*., Design optimization of a periodic microstructured array anode for hard x-ray grating interferometry. *Phys. Med. Biol.* **64**, 145011 (2019).
38. G. Zan *et al*., Quantitative analysis of a micro array anode structured target for hard x-ray grating interferometry. *Phys. Med. Biol.* **65**, 035008 (2020).
39. D. Grider, A. Wright, P. Ausburn, Electron beam melting in microfocus x-ray tubes. *J. Phys. D Appl. Phys.* **19**, 2281 (1986).
40. T. Weitkamp *et al*., X-ray phase imaging with a grating interferometer. *Opt. Express* **13**, 6296–6304 (2005).
41. T. Thüring *et al*., Sensitivity in X-ray grating interferometry on compact systems. *AIP Conf. Proc.* **1466**, 293 (2012).
42. T. Thüring *et al*., Compact hard x-ray grating interferometry for table top phase contrast micro CT. *Proc. SPIE* **8668**, 866813 (2013).
43. Y. Sasano *et al*., Distinctive expression of extracellular matrix molecules at mRNA and protein levels during formation of cellular and acellular cementum in the rat. *His-tochem. J.* **33**, 91–99 (2001).
44. B. L. Foster, Methods for studying tooth root cementum by light microscopy. *Int. J. Oral Sci.* **4**, 119–128 (2012).
45. I. Zanette *et al*., Trimodal low-dose X-ray tomography. *Proc. Natl. Acad. Sci. U.S.A.* **109**, 10199–10204 (2012).
46. M. J. Berger, J. S. Coursey, M. A. Zucker, J. Chang, ESTAR, PSTAR, and ASTAR: Com-puter Programs for Calculating Stopping-Power and Range Tables for Electrons, Protons, and Helium Ions (Version 2.0.1, National Institute of Standards and Tech-nology, Gaithersburg, MD, 2005).
47. S. Agostinelli *et al*., GEANT4—A simulation toolkit. *Nucl. Instrum. Meth. A.* **506**, 250–303 (2003).
48. T. Donath *et al*., Inverse geometry for grating-based X-ray phase-contrast imaging. . *J. Appl. Phys.* **106**, 054703 (2009).
49. A. Momose, H. Kuwabara, W. Yashiro, X-ray phase imaging using Lau Effect. *Appl. Phys. Express* **4**, 066603 (2011).
50. F. Pfeiffer, C. Kottler, O. Bunk, C. David, Hard x-ray phase tomography with low-brilliance sources. *Phys. Rev. Lett.* **98**, 108105 (2007).

APPLIED PHYSICAL SCIENCES